



**Mixed Proton–electron–oxide Ion Triple Conducting  
Manganite as Efficient Cobalt-free Cathode for Protonic  
Ceramic Fuel Cells**

Journal:	<i>Journal of Materials Chemistry A</i>
Manuscript ID	TA-ART-04-2020-003899.R1
Article Type:	Paper
Date Submitted by the Author:	07-May-2020
Complete List of Authors:	Wang, Ning; Hokkaido University, Hinokuma, Satoshi; National Institute of Advanced Industrial Science and Technology (AIST), Interdisciplinary Research Center for Catalytic Chemistry Ina, Toshiaki; Japan Synchrotron Radiation Research Institute, Research and Utilization Division zhu, chunyu; Hokkaido University Habazaki, Hiroki; Hokkaido University, Aoki, Yoshitaka; Hokkaido University, Faculty of Engineering

## ARTICLE

# Mixed Proton–electron–oxide Ion Triple Conducting Manganite as Efficient Cobalt-free Cathode for Protonic Ceramic Fuel Cells

Ning Wang,<sup>a</sup> Satoshi Hinokuma,<sup>b</sup> Toshiaki Ina,<sup>c</sup> Chunyu Zhu,<sup>d</sup> Hiroki Habazaki<sup>d</sup> and Yoshitaka Aoki<sup>\*d</sup>

Received 00th January 20xx,  
Accepted 00th January 20xx

DOI: 10.1039/x0xx00000x

It is challenging for materials chemists to develop efficient, cobalt-free cathode materials for solid oxide fuel cells mainly because of the resource scarcity. This study demonstrates that a cubic-type  $\text{La}_{0.7}\text{Sr}_{0.3}\text{Mn}_{0.7}\text{Ni}_{0.3}\text{O}_{3-\delta}$  (C-LSMN7373) perovskite is promising for intermediate-temperature protonic ceramic fuel cells (PCFCs) because of the sufficient  $\text{H}^+/\text{e}^-/\text{O}^{2-}$  triple conductivity. The oxide can be hydrated by gaining 0.1 molar fraction  $\text{H}_2\text{O}$  under wet air at 415 °C, as confirmed by thermogravimetry analysis. An *in situ* extended X-ray absorption fine structure (EXAFS) analysis shows that the hydration reaction takes place via the association between  $\text{H}_2\text{O}$  and oxygen vacancy, coupled with the redox of Mn and O atoms. Rhombohedral-type  $\text{La}_{0.7}\text{Sr}_{0.3}\text{Mn}_{1-x}\text{Ni}_x\text{O}_{3-\delta}$  cannot undergo hydration because the oxygen vacancy concentration required for water association is lower than the cubic phase concentration. The cathode performances of various PCFCs are examined by fabricating thin-film cells based on a  $\text{Ba}(\text{Zr}_{0.4}\text{Ce}_{0.4}\text{Y}_{0.2})\text{O}_3$  electrolyte. The peak power density of the PCFCs with cubic-type LSMN7373 cathode is 386  $\text{mW cm}^{-2}$  at 600 °C, which is much higher than the reported values for the Zr-rich side electrolytes. Moreover, the cathodic polarization resistance is lower than that of the cell with the widely used  $\text{La}_{0.6}\text{Sr}_{0.4}\text{Co}_{0.2}\text{Fe}_{0.8}\text{O}_3$  cathode below 550 °C.

## 1 Introduction

Protonic ceramic fuel cells (PCFCs) based on protonic conducting electrolytes have more advantages at operating temperatures below 600 °C than solid oxide fuel cells (SOFCs) because the activation energy required for proton conduction (0.3–0.6 eV) is lower than that required for oxide ion conduction (0.8 eV), which is key to lowering fuel cell costs and extending lifetimes.<sup>1–7</sup> Although thin-film PCFCs can exhibit very high power output (> 1.0  $\text{W cm}^{-2}$ ) at 600 °C,<sup>8–10</sup> their performance rapidly deteriorates with further reduction in the operating temperature; at 500 °C, the peak power density is limited to approximately 0.5  $\text{W cm}^{-2}$ .<sup>8,10,11</sup> A key reason for this low performance is the lack of suitable cathode materials that promote the association between protons and oxide ions via oxygen reduction reaction in PCFCs.<sup>12–20</sup> Due to the different cathode reaction mechanisms, it is not rational to directly use the cathode that performs well for oxygen-ion conducting solid oxide fuel cells (SOFCs) for PCFCs, although this approach is widely used in the early development stage of PCFCs.

Ideal cathodes for PCFCs should exhibit triple conduction of oxide ions, protons and electrons, because such a triple-

conducting oxide can extend the reaction zones beyond the gas-electrode-electrolyte triple phase boundary (TPB) and thus reduce the cathodic overpotential.<sup>3,21</sup> Although many cathode materials possess oxide ion and electron mixed conductivity, the introduction of proton-conduction in the cathode has remained challenging for many years.<sup>6–8</sup> Generally, protons are incorporated into metal oxides through hydration mediated via the association between oxygen vacancies and water molecules. Hence, oxides with emergent hydration properties at elevated temperatures are potential candidates for mixed proton–electron–oxide ion triple conductors. Most of the triple conductors developed recently are focused on cobalt-base oxides with perovskite-related structures.<sup>3,8,17–20</sup>  $\text{BaCo}_{0.4}\text{Fe}_{0.4}\text{Zr}_{0.1}\text{Y}_{0.1}\text{O}_{3-\delta}$  can readily hydrate by taking 0.0095 molar fraction of water at 500 °C under a partial water pressure ( $p_{\text{H}_2\text{O}}$ ) of 0.01 atm; the related cells exhibit a relatively high power gain (0.46  $\text{W cm}^{-2}$ ) at 500 °C.<sup>3</sup> Double perovskite-type  $\text{PrBa}_{0.5}\text{Sr}_{0.5}\text{Co}_{1.5}\text{Fe}_{0.5}\text{O}_{5+\delta}$  is also capable of having proton defects equaling 0.017 molar fractions at 600 °C;<sup>8</sup> moreover, the PCFCs implementing the oxide in the electrolyte/cathode interlayer achieves the highest power outputs of PCFCs at 500 °C.<sup>8,25</sup> In spite of the high performance of cobalt-containing cathodes, however, it is still demanded to develop Co-free alternatives because of the relatively high reactivity, resource scarcity, and cost of Co oxides.<sup>26</sup>

Manganese base perovskites, i.e.  $\text{La}_{1-x}\text{Sr}_x\text{MnO}_3$  have been recognized to poorly-active cathode materials for PCFC in comparison to cobalt base oxides.<sup>27–33</sup> This family takes rhombohedral structure at high temperature, but the metastable phase prepared low temperature root tends to take cubic structure.<sup>34,35</sup> More recently, Wang *et al.* reported that

<sup>a</sup> Graduate School of Chemical Sciences and Engineering, Hokkaido University, N13W8, Kita-ku, Sapporo, 060-8628, Japan.

<sup>b</sup> National Institute of Advanced Industrial Science and Technology (AIST), Central 5-2, 1-1-1 Higashi, Tsukuba, Ibaraki, 305-8565, Japan.

<sup>c</sup> Japan Synchrotron Radiation Research Institute (JASRI), 1-1-1, Kouto, Sayo-cho, Sayo-gun, Hyogo, 679-5198, Japan

<sup>d</sup> Faculty of Engineering, Hokkaido University, N13W8, Kita-ku, Sapporo, 060-8628, Japan.

Electronic Supplementary Information (ESI) available: [details of any supplementary information available should be included here]. See DOI: 10.1039/x0xx00000x

cubic-type perovskite  $\text{La}_{0.7}\text{Sr}_{0.3}\text{MnO}_{3-\delta}$  could be hydrated in wet air by retaining about 0.07 molar fraction of water at approximately 400 °C.<sup>35</sup> In this case, the thermochemical hydration reaction is driven by the association between oxygen vacancy and water, mediated via the bulk diffusion of proton and oxide ions.<sup>35</sup> Therefore, cubic-type  $\text{La}_{0.7}\text{Sr}_{0.3}\text{MnO}_{3-\delta}$  is a potential Co-free,  $\text{H}^+/\text{e}^-/\text{O}^{2-}$  triple conducting cathodic material for advanced PCFCs owing to its sufficient proton conductivity at intermediate temperatures. Herein, we demonstrate that cubic-type  $\text{La}_{0.7}\text{Sr}_{0.3}\text{MnO}_{3-\delta}$  and its derivatives  $\text{La}_{0.7}\text{Sr}_{0.3}\text{Mn}_{1-x}\text{Ni}_x\text{O}_{3-\delta}$  (LSMN;  $x = 0.1$  and  $0.3$ ) can help significantly lower the cathodic polarization resistance of Zr-rich side  $\text{BaZr}_{0.4}\text{Ce}_{0.4}\text{Y}_{0.2}\text{O}_3$ -base PCFCs. The aliovalent substitution of  $\text{Mn}^{4+}$  with  $\text{Ni}^{3+}$  sufficiently improves the hydration capacity of  $\text{La}_{0.7}\text{Sr}_{0.3}\text{MnO}_{3-\delta}$  owing to increased oxygen vacancies for water association. Thus, the  $\text{La}_{0.7}\text{Sr}_{0.3}\text{Mn}_{1-x}\text{Ni}_x\text{O}_{3-\delta}$  cathode, including the widely-used  $\text{La}_{0.6}\text{Sr}_{0.4}\text{Co}_{0.2}\text{Fe}_{0.8}\text{O}_3$  (LSCF6428), exhibits low cathodic polarization resistance at intermediate temperatures. This confirms their applicability as a cobalt-free PCFC cathodic material.

## 2 Results and discussion

### 2.1 Preparation of LSMN

**Fig. 1** shows the XRD patterns of  $\text{La}_{0.7}\text{Sr}_{0.3}\text{Mn}_{1-x}\text{Ni}_x\text{O}_{3-\delta}$  (LSMN;  $x = 0.1$  and  $0.3$ ), which are denoted hereinafter by LSMN7391 and LSMN7373, respectively. First, single cubic-perovskite phases of LSMN7391 and LSMN7373 were obtained by annealing (800 °C for 15 h in pure  $\text{O}_2$ ) based on our previous report;<sup>35</sup> these are called C-LSMN7391 and C-LSMN7373, respectively. Both C-LSMN7391 and C-LSMN7373 completely transform to a rhombohedral phase (*R*) after annealing at 1000 °C under pure  $\text{O}_2$  for 15 h, as confirmed by a Rietveld analysis conducted previously.<sup>35</sup> The rhombohedral LSMN oxides are abbreviated as R-LSMN7391 and R-LSMN7373.

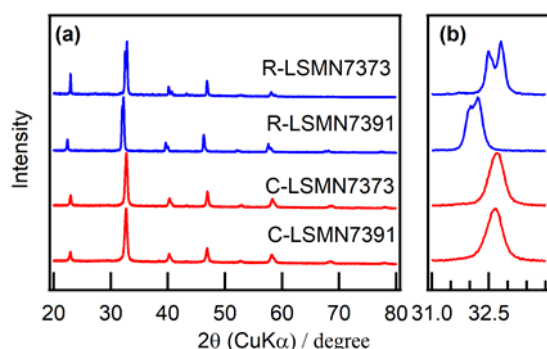


**Fig. 1** (a) XRD patterns of cubic- and rhombohedral-type  $\text{La}_{0.7}\text{Sr}_{0.3}\text{Mn}_{1-x}\text{Ni}_x\text{O}_{3-\delta}$  ( $x = 0.1$ , and  $0.3$ ). (b) Expansion of (110) peaks for cubic phase, and (110) and (104) peaks for rhombohedral phase.

### 2.2 Thermochemical hydration/dehydration reactions of LSMN

**Figs. 2a–d** show the thermogravimetric (TG) curves of the C-LSMN samples, measured at temperatures ranging from room

temperature (RT, 30 °C) to 1000 °C under dry and wet Ar (including 10 ppm of  $\text{O}_2$  additive) and air. (In the discussion hereinafter, the Ar gas includes 10 ppm of  $\text{O}_2$ ). Both C-LSMN7391 and C-LSMN7373 exhibit three steps of thermal weight losses both in Ar and in air. The weight losses at  $T < 200$  °C and at approximately 700 °C can be attributed to the desorption of surface  $\text{H}_2\text{O}$  and the lattice oxygen loss with the reduction from  $\text{Mn}^{4+}$  to  $\text{Mn}^{3+}$ ,<sup>36</sup> respectively. C-LSMN exhibits a clear mass loss at approximately 400 °C, probably because of the dehydration following the release of bulk  $\text{H}_2\text{O}$ .<sup>35</sup> The onset temperature corresponding to the clear mass loss is 350 °C in dry atmosphere and it increases to 402, 411, and 430 °C when increasing the water partial pressure ( $p_{\text{H}_2\text{O}}$ ) to 0.003, 0.009, and 0.023, respectively, for C-LSMN7373 (**Fig. 3a**). The onset temperatures are not sensitive to the oxygen partial pressure ( $p_{\text{O}_2}$ ): the clear mass loss starts at 350 °C in dry air and at 430 °C in wet air ( $p_{\text{H}_2\text{O}} = 0.023 p_0$ ), which are the same as those in dry and wet Ar ( $p_{\text{H}_2\text{O}} = 0.023 p_0$ ), respectively (Figs. 2c and d). These characteristics prove that the mass losses at approximately 400 °C are related to thermochemical dehydration reactions. In contrast, the corresponding rhombohedral phases, namely R-LSMN7391 and R-LSMN7373, do not show apparent weight losses in the temperature range of 200–700 °C in dry and wet atmospheres (Figs. 2e–h), indicating that the rhombohedral phase does not undergo enhanced hydration when  $p_{\text{H}_2\text{O}} = 0.023 p_0$ .

To verify the capability of reversible proton uptake and release through thermochemical hydration/dehydration reactions, the mass changes are monitored at 415 °C by repeatedly switching between dry and wet ( $p_{\text{H}_2\text{O}} = 0.023 p_0$ ) atmospheres every 30 mins, as shown in Figs. 3c–f. C-LSMN exhibits reversible mass changes when dry/wet switching in both Ar and air atmospheres (Figs. 3c–f), with a mass gain on exposure to wet gases ( $p_{\text{H}_2\text{O}} = 0.023 p_0$ ) and an equal mass loss when exposed to dry gases. Here, the weight variable ( $\Delta W$ ) is defined as the mean weight difference between the samples equilibrated in dry and wet conditions for five switching cycles. C-LSMN7391 exhibits  $\Delta W$  of approximately 0.40 and 0.44 wt% in wet Ar and air, respectively (Table 1; Figs. 3c and e), and C-LSMN7373 exhibits  $\Delta W$  of 0.64 wt% in Ar and 0.78 wt% in air (Table 1; Figs. 3d and f); the latter values are higher than those of C-LSMN73 (0.5 wt%).<sup>35</sup> The hydration/dehydration cycles are completely repeatable, because the mass loss during dehydration and mass gain during hydration agree within 10%. As for R-LSMN, the TG curves at 415 °C are almost flat as the Ar/air is changed between dry and wet conditions (**Fig. S1**), which is in accordance with the unapparent weight losses in the temperature range of 200–700 °C in both dry and wet atmospheres (Figs. 2e–h).

The  $\Delta W$  value of C-LSMN7373 is very sensitive to  $p_{\text{H}_2\text{O}}$ ; the values decrease from 0.78 wt% to 0.33 wt% to 0.07 wt% when  $p_{\text{H}_2\text{O}}$  is decreased from 0.023 to 0.009 to 0.003 in wet air (Fig. 3b). This shows that C-LSMN can undergo thermochemical hydration reactions even at elevated temperatures.

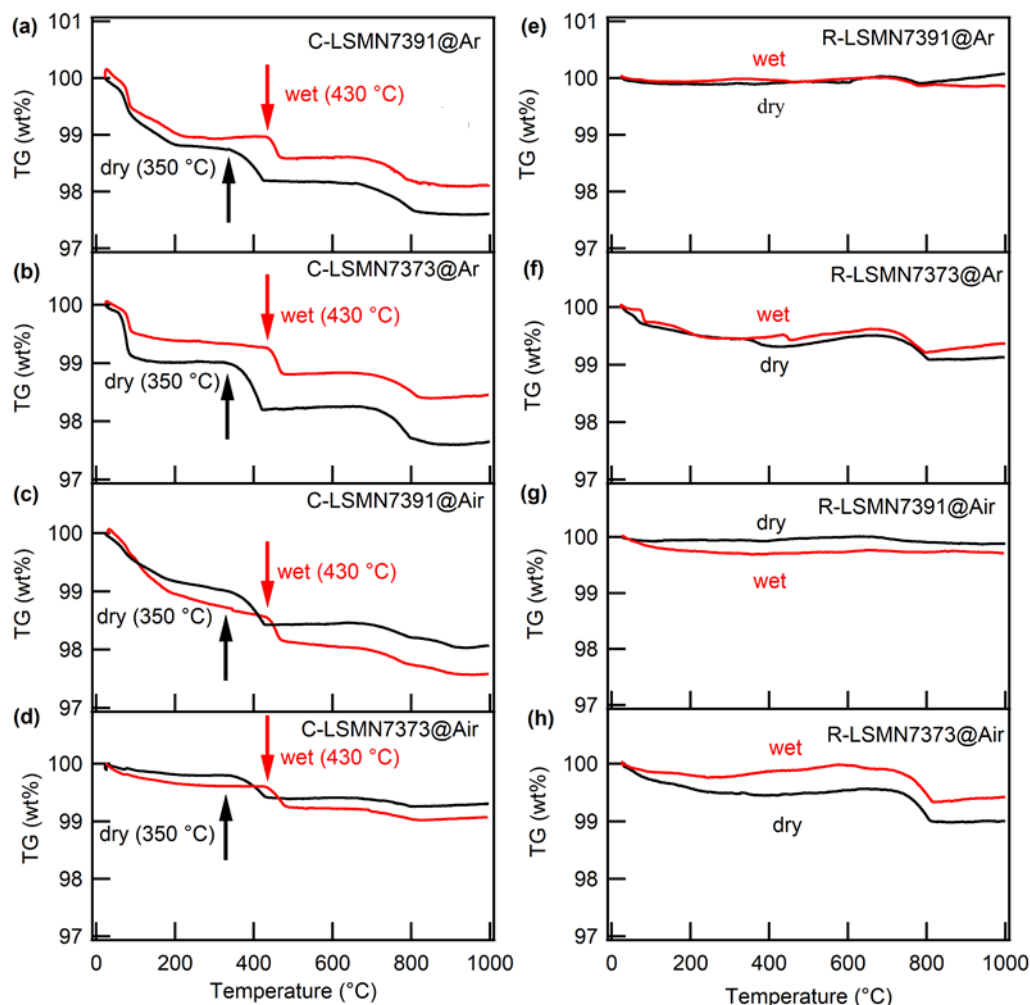
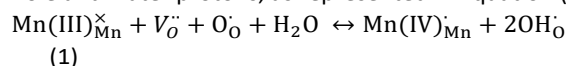


**Fig. 2** TG curves measured at temperatures ranging from RT to 1000 °C in dry and wet Ar (10 ppm O<sub>2</sub> additive) (a, b, e, f) and air (c, d, g, h) for C-LSMN7391, C-LSMN7373, and R-LSMN7391, R-LSMN7373. In (a)–(d), the black and red arrows indicate the onset temperatures for dehydration in dry and wet atmospheres, respectively.

### 2.3 *In situ* Mn K-edge extended X-ray absorption fine structure (EXAFS) analysis

The hydration/dehydration reactions of C-LSM73 are driven by the coupling of the association between oxygen vacancy and water and the carriers exchange between oxygen hole and water protons, as represented in Equation (1).<sup>35</sup>

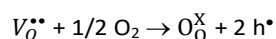


In Equation (1), the Kröger–Vink notation is used, with  $\text{OH}_{\text{O}}^{\bullet}$  being the proton defect,  $\text{O}_{\text{O}}^{\times}$  the oxygen hole,  $\text{Mn(III)}_{\text{Mn}}^{\times}$  Mn(III) cations on Mn site,  $\text{Mn(IV)}_{\text{Mn}}^{\bullet}$  Mn(IV) cations on Mn site, and  $V_{\text{O}}^{\bullet\bullet}$  the oxygen vacancy.

In proton-conducting ceramic electrolytes, such as  $\text{BaZr}_{1-x-y}\text{Ce}_x\text{Y}_y\text{O}_3$ , the proton carriers are incorporated via the association between oxygen vacancies and water molecules, as represented in Equation (2).<sup>12,37,38</sup>



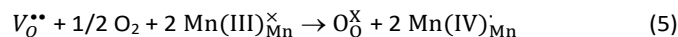
Here,  $\text{O}_{\text{O}}^{\times}$  is the lattice oxygen. In metal oxides, the association between oxygen vacancies and oxygen gas is in equilibrium.



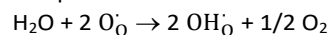
Here,  $h^{\bullet}$  is an electron hole. If the hole carriers are incorporated into the valence band comprising mainly of O 2p states, Equation (3) can be rewritten with an oxygen hole ( $\text{O}_{\text{O}}^{\times}$ ).<sup>39,40</sup>



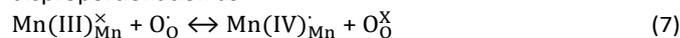
In the case of LSM, the association between  $V_{\text{O}}^{\bullet\bullet}$  and O<sub>2</sub> gas involves valence change in Mn cations.<sup>41</sup> Therefore, reaction (2) can be modified as follows:



The proton and hole carriers are in equilibrium as follows.



Coupling Equations (4) and (6) gives Equation (2). Moreover, combining Equations (4) and (5) yields the charge disproportionation as



Therefore, Equation (1) can be interpreted by coupled reactions of the water–vacancy association (equation (2)) and the charge disproportionation (equation (7)). In fact, we demonstrated the

valence change of O and Mn atoms for the hydration of C-LSMN73 by means of synchrotron X-ray adsorption spectroscopy.<sup>35</sup>

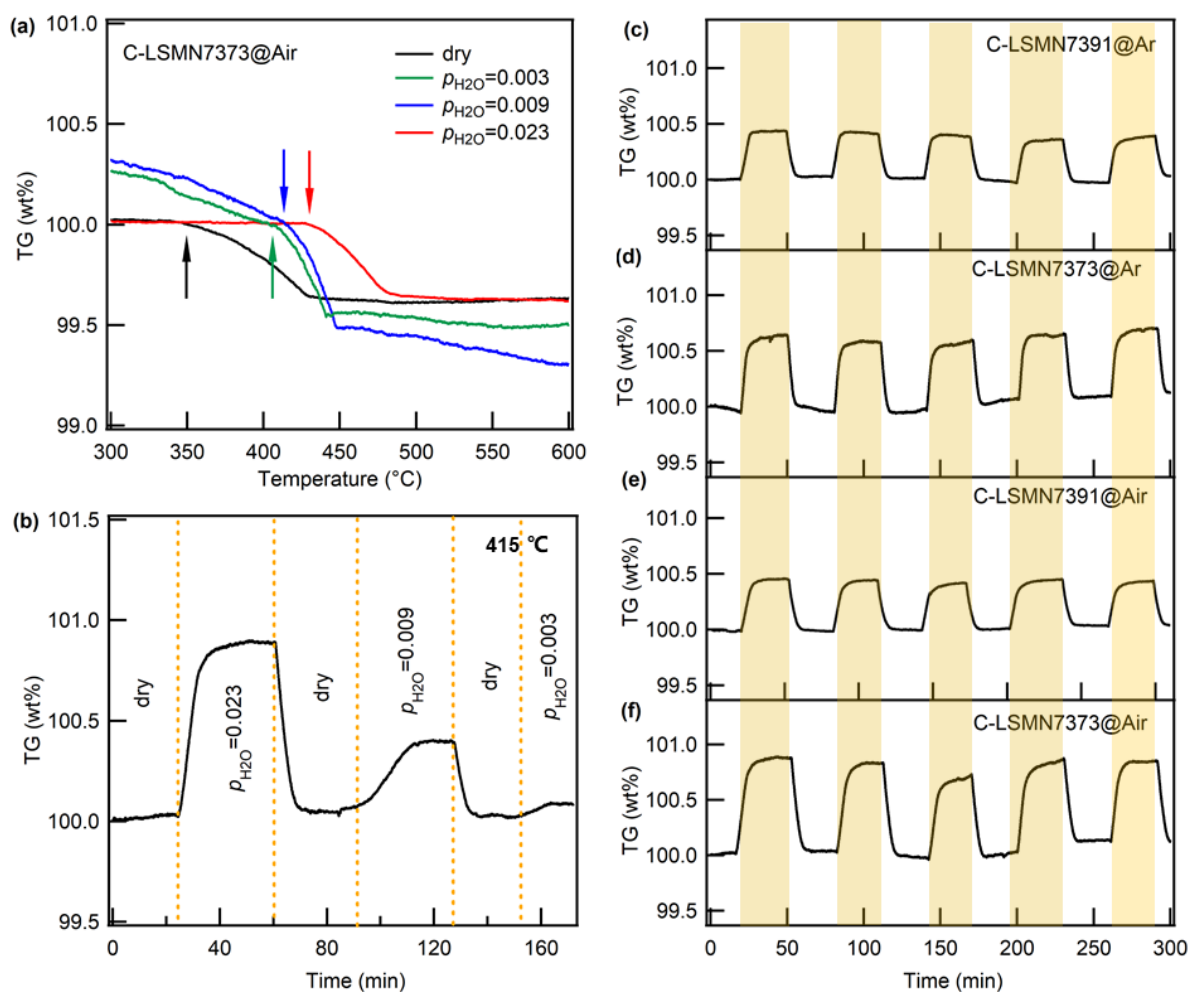


**Fig. 3** (a) TG curves of C-LSMN7373 under wet air atmosphere with different  $p_{\text{H}_2\text{O}}$ . Here, '100 wt%' of the TG curves was set at the weight of onset temperatures of releasing bulk water for the comparison. In (a), the arrows indicate the onset temperature to start dehydration. (b) Weight gain/loss in response to atmospheric switching between wet/dry air every 30 mins at 415 °C for C-LSMN7373 with different  $p_{\text{H}_2\text{O}}$ . Weight gain/loss of C-LSMN7391 and C-LSMN7373 in response to atmospheric switching between wet/dry Ar (c, d) and air (e, f) every 30 mins at 415 °C. The pale-yellow areas represent the duration for which the samples were under wet atmosphere.

To elucidate the average Mn valence state change and local structure rearrangements by hydration/dehydration reactions with the charge disproportionation, an extended X-ray absorption fine structure (EXAFS) analysis was conducted for LSMN oxides with the reference samples of  $\text{LaMnO}_3$  and  $\text{CaMnO}_3$ . **Fig. S2** shows the normalized absorption in the X-ray adsorption near edge structure (XANES) region of the pristine C-LSMN and R-LSMN samples, along with the reference samples of  $\text{LaMnO}_3$  and  $\text{CaMnO}_3$  at 415 °C. These oxides exhibit a weak pre-edge peak at approximately 6540 eV (**Fig. S2**), attributed to the electric dipole forbidden transition of  $1s$  electron to an unoccupied  $3d$  orbital, and subsequently, yield a vertically rising main edge with a maximum peak at approximately 6553 eV

corresponding to the electron transition from  $1s$  to  $4p$  orbitals.<sup>35,42</sup> In the  $K$ -edge XANES of manganese oxides, the adsorption edge shifts to higher energy in proportion to the average Mn valence states, since the core electron binding energy linearly increases with the positive charges on the cations.<sup>43,44</sup> Hence, a relative shift in comparison to reference materials, called the chemical shift, allows determining the average Mn valence states of these oxides if the crystal structures are analogous each other.<sup>44-46</sup> Previously, we evaluated the Mn valence state in perovskite-type  $\text{La}_{1-x}\text{Sr}_x\text{MnO}_{3-\delta}$  series by combining the iodometry for a quenched sample and the chemical shifts of the Mn  $K$ -edge XANES,<sup>35</sup> confirming that Mn  $K$ -edge monotonically increases in proportion to the

oxidation states of Mn cations; thus, the valence states could be properly determined with the calibration lines prepared by LaMnO<sub>3</sub> and CaMnO<sub>3</sub> references. Based on this, the Mn valence state of La<sub>1-x</sub>Sr<sub>x</sub>Mn<sub>1-y</sub>Ni<sub>y</sub>O<sub>3-δ</sub> was determined from the chemical shift of Mn K-edge by fixing the Mn valence states of LaMnO<sub>3</sub>

and CaMnO<sub>3</sub> references at 415 °C in dry air to +3.20 and +3.99, respectively.<sup>35,47</sup>

**Table 1.** Hydration properties of C-LSMN and other triple conductors.

Systems	ΔW (wt%)	Δn <sup>a</sup>	[OH <sup>o</sup> ] <sup>b</sup>	Temperature (°C)	p <sub>H2O</sub> (atm)	Ref.
C-La <sub>0.7</sub> Sr <sub>0.3</sub> Mn <sub>0.9</sub> Ni <sub>0.1</sub> O <sub>2.93</sub>	0.44 (air)	0.055 (air)	0.110 (air)	415	0.023	This work
	0.40 (Ar)	0.051 (Ar)	0.102 (Ar)			
C-La <sub>0.7</sub> Sr <sub>0.3</sub> Mn <sub>0.7</sub> Ni <sub>0.3</sub> O <sub>2.94</sub>	0.78 (air)	0.098 (air)	0.196 (air)	415	0.023	This work
	0.64 (Ar)	0.080 (Ar)	0.160 (Ar)			
C-La <sub>0.7</sub> Sr <sub>0.3</sub> Mn <sub>0.7</sub> Ni <sub>0.3</sub> O <sub>2.94</sub>	0.33 (air)	0.042 (air)	0.084 (air)	415	0.009	This work
C-La <sub>0.7</sub> Sr <sub>0.3</sub> Mn <sub>0.7</sub> Ni <sub>0.3</sub> O <sub>2.94</sub>	0.07 (air)	0.008 (air)	0.016 (air)	415	0.003	This work
C-La <sub>0.7</sub> Sr <sub>0.3</sub> MnO <sub>2.95</sub>	0.56 (air)	0.071 (air)	0.142 (air)	415	0.023	35
	0.51 (Ar)	0.064 (Ar)	0.128 (Ar)			
PrBa <sub>0.5</sub> Sr <sub>0.5</sub> Co <sub>1.5</sub> Fe <sub>0.5</sub> O <sub>5+δ</sub>	-	0.018	0.036	200	0.02	8
Ba <sub>0.95</sub> La <sub>0.05</sub> Fe <sub>0.8</sub> Zn <sub>0.2</sub> O <sub>3-δ</sub>	-	0.050	0.10	200	0.016	56
BaCo <sub>0.4</sub> Fe <sub>0.4</sub> Zr <sub>0.2</sub> O <sub>3-δ</sub>	-	-	0.015-0.05	200-400	0.015	57
Ba <sub>0.5</sub> Sr <sub>0.5</sub> Fe <sub>0.8</sub> Zn <sub>0.2</sub> O <sub>3-δ</sub>	-	-	0.015	350	0.02	58
Ba <sub>0.5</sub> Sr <sub>0.5</sub> Fe <sub>0.8</sub> Zn <sub>0.2</sub> O <sub>3-δ</sub>	-	-	0.02	400	0.02	58
Ba <sub>0.5</sub> Sr <sub>0.5</sub> Fe <sub>0.8</sub> Zn <sub>0.2</sub> O <sub>3-δ</sub>	-	-	0.013-0.032	350-600	0.02	58
PrBa <sub>0.5</sub> Sr <sub>0.5</sub> Co <sub>1.5</sub> Fe <sub>0.5</sub> O <sub>5+δ</sub>	-	0.009	0.018	600	0.02	8
Ba <sub>0.95</sub> La <sub>0.05</sub> Fe <sub>0.8</sub> Zn <sub>0.2</sub> O <sub>3-δ</sub>	-	0.023	0.046	400	0.016	56
Ba <sub>0.95</sub> La <sub>0.05</sub> Fe <sub>0.8</sub> Zn <sub>0.2</sub> O <sub>3-δ</sub>	-	0.012	0.024	500	0.016	56
BaCo <sub>0.4</sub> Fe <sub>0.4</sub> Zr <sub>0.1</sub> Y <sub>0.1</sub> O <sub>3-δ</sub>	-	0.095	0.019	500	0.0095	3

a: Represented by molar fraction; b: Given by twice of Δn.

**Figs. 4a–d** show the normalized absorption in the XANES region of C-LSMN and R-LSMN, measured during dry/wet atmosphere switching in air at 415 °C. The absorption edge positions of C-LSMN7391 and C-LSMN7373 shift from 6549.98 and 6550.28 eV to 6550.22 and 6550.78 eV, respectively, when switching from dry to wet air (Figs. 4a and b), resulting in an increase in the average Mn valence state from 3.17 and 3.26 to 3.24 and 3.40 for C-LSMN7391 and C-LSMN7373, respectively (Fig. 4i). However, R-LSMN7391 and R-LSMN7373 do not exhibit chemical shifts throughout the dry/wet switching (Figs. 4c and d), and thus, their average Mn valence states remain at 3.31 and 3.39, respectively, (Fig. 4i and Table 2).

The Ni K-edge XANESs for C- and R-LSMN at 415 °C in dry air overlap with each other, and their adsorption edge positions are higher than that of NiO but identical to that of LaNiO<sub>3</sub> reference, indicating that Ni nominally takes +3 valence state in all LSMN regardless of the structure (cubic or rhombohedral) (Fig. S4). In addition, the *in situ* Ni K-edge XANES spectra show that Ni does not change to a higher valence state via hydration (Fig. S5), confirming Ni cations of all LSMN remain in 3+ valence state throughout the hydration/dehydration reaction at approximately 400 °C. We conclude that C-LSMN undergoes hydration/dehydration coupled with Mn redox by Equation (1) as is the case with the corresponding reaction of C-LSM73.<sup>35</sup>

**Figs. 4e–h** show the radial distribution function (RDF) obtained from the Fourier transform EXAFS. For the LSMN oxides, the first coordination shells corresponding to an intense peak in the range of approximately 1.6–2.0 Å can be attributed to the shortest shell of Mn–O bond, and the second and the third shells distributed in the range of 2.0–4.0 Å can be assigned to the coherence in Mn–La or Mn–Sr and in Mn–Mn.<sup>35</sup> The curve fitting analysis to the first Mn–O coordination shell of C-LSMN converged well when using the atomic coordinates of cubic or rhombohedral perovskite LaMnO<sub>3</sub> as an initial set, yielding a Mn–O distance (*r*) of approximately 1.9 Å. It has been widely recognized that EXAFS normally underestimates *CN* around metal atoms because of the annihilation by other heavy atoms and large contribution of Debye-Waller factor.<sup>48</sup> Meanwhile, the *CN* around Mn exhibits the apparent trend of increasing by hydration: the values of C-LSMN7391 and C-LSMN7373 change from 5.04±0.55 and 4.98±0.62 to 5.24±0.47 and 5.21±0.56, respectively (Fig. 4k; Table 2). Regardless of the relatively large errors, these results imply that oxygen vacancies of the C phase decrease via hydration. This feature is also supported by Rietveld refinement on powder XRD patterns, because the site occupancy of O atoms significantly increases by hydration in C phase with the lattice shrinkage due to the increase in Coulombic attraction between oxide and metal ions<sup>36</sup> (Fig. S6; Table S1 and S2).

Un-hydrated *R* phase (*R*-LSMN7391 and *R*-LSMN7373) maintains *CN* at a constant value ( $5.43 \pm 0.74$  (0.61) and  $5.00 \pm 0.50$  (0.72), respectively) irrespective of the humidity (Figs. 4k and Table 2). These results prove that  $\text{H}_2\text{O}$  is incorporated by the association between water molecules and oxygen vacancies according to equation (1).

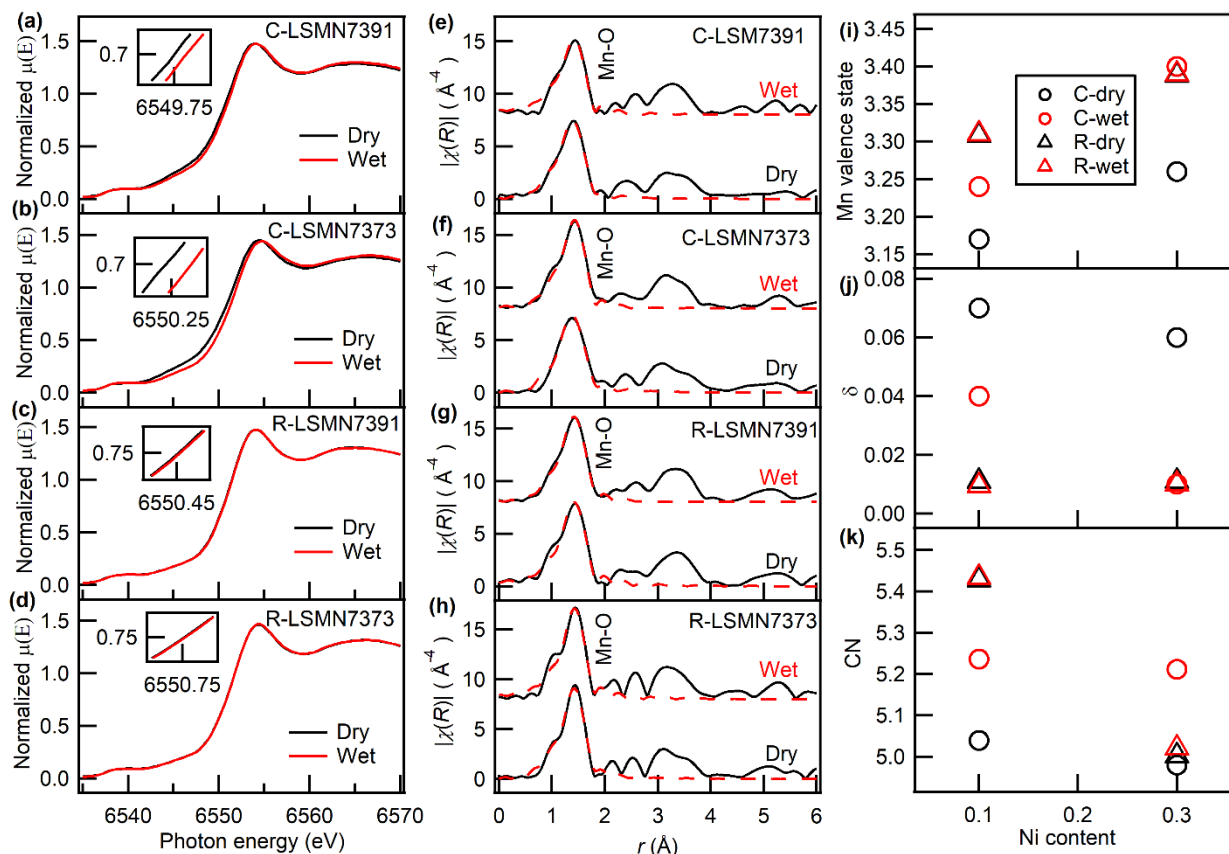


**Fig. 4** *In situ* Mn *K*-edge XANES spectra of C-LSMN7391 (a), C-LSMN7373 (b), *R*-LSMN7391 (c), and *R*-LSMN7373 (d) in a cycle of dry and wet air supplied at 415 °C. Insets of (a)–(c) show the enlarged absorption edge region. Radial distribution functions obtained by Fourier transforming the EXAFS at 415 °C under dry air for C-LSMN7391 (e), C-LSMN7373 (f), *R*-LSMN7391 (g), and *R*-LSMN7373 (h). In (e)–(h), the black and red lines indicate the observed and curve-fitting profiles to the 1st coordination shell (Mn-O), respectively. Average Mn valence state determined from the chemical shift of absorption edges depicted in (a–d) (i). Oxygen deficiency ( $\delta$ ) calculated from the valence states of cations (j). Oxygen-coordination number (*CN*) of Mn cations determined by EXAFS fitting analysis depicted in (e–h) (k). In (i)–(k), the circular and triangular symbols indicate cubic and rhombohedral phases, and the black and red colors help distinguish between dry and wet atmospheres, respectively.

The oxidation states of Mn cations in LSMN oxides were also examined by iodometry. For the analysis, all powder specimens were once annealed in dry and wet air at 415 °C for 6 h, quenched in desiccator, and immediately dissolved into 0.1 M HCl solutions. The chemical analysis results in Mn valence states equaling to 3.25 and 3.33 for C-LSMN7391 in dry and wet air, respectively, and 3.35 and 3.37 for the corresponding *R* phase in dry and wet air, respectively (Fig. S3 and Table 2). Similarly, it gives 3.32 and 3.44 for C-LSMN7373 in dry and wet air, respectively, and 3.45 and 3.48 for the *R* phase in dry and wet air, respectively. These values are in close agreement with ones determined by Mn *K*-edge XANES, which validates the results of EXAFS measurements.

Oxygen vacancies are crucial to hydration/dehydration reactions according to Equation (1). EXAFS and iodometry analysis verify that cubic phase possesses sufficient amount of oxygen vacancies in dry atmosphere. Oxygen deficiency ( $\delta$ ) in  $\text{La}_{0.7}\text{Sr}_{0.3}\text{Mn}_{1-x}\text{Ni}_x\text{O}_{3-\delta}$  is roughly calculated with the Mn valence state determined by XANES and iodometry, assuming that the net charges on La, Sr, Ni, and O are fixed at +3, +2, +3, and –2, respectively (Figs. 4j and S3). Iodometry confirmed that  $\delta$  in dry air (0.03) is almost equivalent with one in dry Ar (0.02) for C-LSMN7391, meaning that  $\delta$  is not sensitive to  $p_{\text{O}_2}$ . Several groups have also reported that  $\delta$  of  $\text{La}_{0.7}\text{Sr}_{0.3}\text{MnO}_{3-\delta}$  (LSM73) remains unchanged with  $p_{\text{O}_2}$ , keeping nearly 0 in the  $p_{\text{O}_2}$  region from  $10^5$  to 0.1 Pa at temperatures below 600 °C.<sup>47,49</sup> This would be due to the relatively large value of oxygen vacancy

formation enthalpy ( $\Delta H \sim 115 \text{ kJ mol}^{-1}$ ),<sup>49</sup> which results in very small value of  $\exp(-\Delta H/RT)$  in the relatively low temperature range with a gas constant  $R$ . The  $\delta$  values of dehydrated C-LSMN7391 and C-LSMN7373 are determined to 0.07 and 0.06, respectively, by XANES and to 0.03 and 0.03, respectively, by iodometry (Table 2).

On the other hand, XANES yield relatively small  $\delta$  values ( $\sim 0.01$ ) for both dehydrated R-LSMN7391 and R-LSMN7373,

and, moreover, iodometry indicates the oxygen excess in both  $R$  phase. Thus, they would not undergo hydration because of the low concentration of oxygen vacancies, unlike C-LSMN with abundant oxygen vacancies.

**Table 2.** Analytical results by EXAFS fitting and iodometry.

Samples	Conditions	Mn valence state <sup>c</sup>	$\delta$	CN	$r/\text{\AA}$	DW	Mn valence state (iodometry) <sup>d</sup>	$\delta$ (iodometry) <sup>d</sup>
C-LSMN7391	dry	3.17	0.07	5.04±0.55	1.91	0.008±0.001	3.25	0.03
	wet	3.24	0.04	5.24±0.47	1.90	0.008±0.001	3.33	-0.005
C-LSMN7373	dry	3.26	0.06	4.98±0.62	1.90	0.007±0.002	3.32	0.03
	wet	3.40	0.01	5.21±0.56	1.91	0.007±0.001	3.44	-0.01
R-LSMN7391	dry	3.31	0.01	5.43±0.74	1.91	0.007±0.002	3.35	-0.01
	wet	3.31	0.01	5.43±0.61	1.92	0.008±0.002	3.37	-0.02
R-LSMN7373	dry	3.39	0.01	5.00±0.50	1.90	0.006±0.001	3.45	-0.02
	wet	3.39	0.01	5.02±0.72	1.89	0.006±0.002	3.48	-0.035

<sup>c</sup> Mn Valence state and oxygen deficiency determined by XANES analysis.

<sup>d</sup> Mn Valence state and oxygen deficiency calculated determined by iodometry. The negative sign represents the oxygen excess (for example, -0.005 means the oxygen stoichiometry is 3.005).

## 2.4 Hydration ability of LSMN

The hydration capability ( $\Delta n$ ), which is defined as the molar fraction of water absorbed ( $(n(\text{H}_2\text{O}))$  to  $n(\text{La}_{0.7}\text{Sr}_{0.3}\text{Mn}_{1-x}\text{Ni}_x\text{O}_{3-\delta})$  ( $\Delta n = n(\text{H}_2\text{O}) / n(\text{LSMN})$ ), can be roughly estimated from the  $\Delta W$  values. Here, the molecular formulae of dehydrated C-LSMN7391 and C-LSMN7373 are assumed to be  $\text{La}_{0.7}\text{Sr}_{0.3}\text{Mn}_{0.9}\text{Ni}_{0.1}\text{O}_{2.93}$  and  $\text{La}_{0.7}\text{Sr}_{0.3}\text{Mn}_{0.7}\text{Ni}_{0.3}\text{O}_{2.94}$ , respectively, using  $\delta$  as calculated above. The  $\Delta n$  values of C-LSMN7391 and C-LSMN7373 are 0.055 and 0.098, respectively, in air (Table 1), which are consistent with the values expected from Mn valence changes (0.07 and 0.14 for C-LSMN7391 and C-LSMN7373, respectively; Fig. 4i; Table 2) through hydration/dehydration reactions. The resultant proton concentrations of C-LSMN7391 and C-LSMN7373 are 0.102 and 0.160, respectively, in Ar and 0.11 and 0.196, respectively, in air. Surprisingly, these values are comparable to the proton concentrations of well-known proton conductors  $\text{BaCe}_{0.9}\text{Y}_{0.1}\text{O}_3$  ( $\sim 0.1$ ) and  $\text{BaZr}_{0.9}\text{Y}_{0.1}\text{O}_3$  ( $\sim 0.08$ ) under wet  $\text{N}_2$  atmosphere ( $p_{\text{H}_2\text{O}} = 0.023 \text{ atm}$ ) at  $600 \text{ }^\circ\text{C}$ .<sup>12</sup>

Both C-LSMN7391 and C-LSMN7373 tend to have larger  $\Delta n$  in air rather than that in Ar. Equilibrium constant of equation (1)  $k_1$ , is given by:

$$k_1 = \frac{[\text{Mn}^{4+}] \cdot [\text{OH}_0]_2}{[\text{Mn}^{3+}] \cdot [\text{V}_0^*] \cdot [\text{O}_0] \cdot p_{\text{H}_2\text{O}}} \quad (8)$$

Equilibrium constant of equation (4),  $k_4$ , is given by:

$$k_4 = \frac{[\text{O}_0]_2}{[\text{V}_0^*] \cdot [\text{O}_0^*] \cdot p_{\text{O}_2}} \quad (9)$$

Combined (8) and (9), the proton concentration  $[\text{OH}_0]$  can be represented as follows.

$$[\text{OH}_0]_2 = \frac{k_1 \cdot \sqrt{k_4} \cdot [\text{Mn}^{3+}] \cdot \sqrt{[\text{V}_0^*]^3} \cdot \sqrt{[\text{O}_0^*]} \cdot \sqrt{p_{\text{O}_2}} \cdot p_{\text{H}_2\text{O}}}{[\text{Mn}^{4+}]} \quad (10)$$

In a separate experiment, the  $C$  phase was confirmed to have the same  $[\text{Mn}^{3+}]/[\text{Mn}^{4+}]$  ratio in both Ar and air atmosphere at  $415 \text{ }^\circ\text{C}$  by means of XANES.  $[\text{V}_0^*]$  of LSMN is almost constant in the  $p_{\text{O}_2}$  range from  $10^{-4}$  to  $10^5 \text{ Pa}$  at temperatures below  $600 \text{ }^\circ\text{C}$ , as mentioned above. Hence, equation (10) suggests  $[\text{OH}_0]$  thus increases with  $p_{\text{O}_2}$  at a fixed  $p_{\text{H}_2\text{O}}$  attributed to the increase of  $[\text{O}_0^*]$  in equation (6). This feature is consistent with the observed  $p_{\text{O}_2}$  dependence of  $\Delta n$ . These provide a verification that C-LSMN undergoes bulk hydration by equation (1) coupled of equation (2) and (7).

Fig. 5 shows the transmittance IR spectroscopy of O–H stretching modes of C- and R-LSMN7373 in the wavenumber range of  $3100\text{--}3500 \text{ cm}^{-1}$ , measured at elevated temperatures in wet air. The absorption band of O–H stretching is evident even at  $600 \text{ }^\circ\text{C}$  in C-LSMN7373, however, it disappears at temperatures above  $400 \text{ }^\circ\text{C}$  in the  $R$  phase. Hence the  $C$  phase is confirmed to be hydrated, retaining protonic defects, near the operation temperatures of PCFCs.

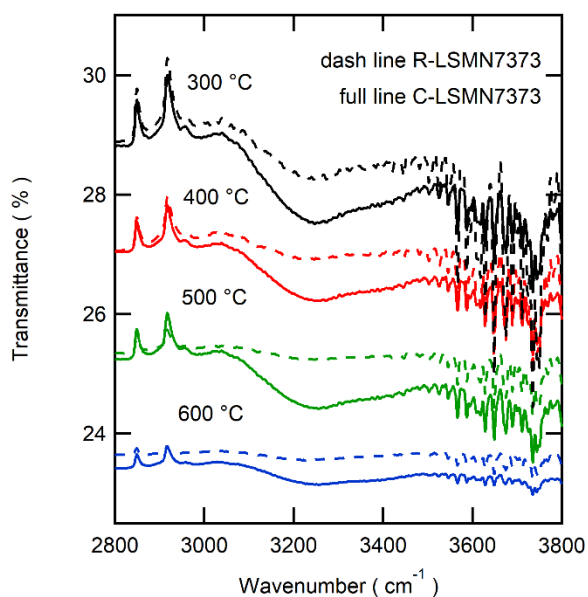


Fig. 5 Transmittance IR spectra of hydroxyl stretching modes for C- and R-LSMN7373 at elevated temperatures (300–600 °C) in wet air. The full and dashed lines indicate C and R phase, respectively.

## 2.5 Performances of LSMN cathodes on PCFCs

The bulk hydration ability of C-LSMN ensures proton conduction at intermediate temperatures, though the conductivity remains unclear. Hence, these oxides are attractive for PCFC cathodes in the intermediate temperature region of 500–600 °C. We examined the performance of PCFCs with C-LSMN porous cathodes by fabricating anode-supported thin film cells based on a  $\text{BaZr}_{0.4}\text{Ce}_{0.4}\text{Y}_{0.2}\text{O}_3$  (BZCY442) electrolyte. The anode/electrolyte half cells were fabricated by single-step co-sintering process (as reported elsewhere); the porous cathode layer was deposited on electrolyte thin films by screen-printing and subsequent annealing at 700 °C.<sup>50</sup> The XRD patterns of the pulverized half cells show no formation of impurity phases on the anode and electrolyte (Fig. S7). The grain size of highly dense BZCY442 electrolytes is approximately 7  $\mu\text{m}$  (Fig. S8a), and their thickness is approximately in the range of 18–19  $\mu\text{m}$  for the measured cells (Fig. S8c). The anode maintains good porosity to provide enough sites for hydrogen reduction (Fig. S8b). For comparison, we examined the cells with C-LSM73 and  $\text{La}_{0.6}\text{Sr}_{0.4}\text{Co}_{0.2}\text{Fe}_{0.8}\text{O}_3$  (LSCF6428) cathodes on BZCY442 based anode-supported cells with largely the same electrolyte thickness. The SEM images of these cathodes (Fig. S9) were taken after they were annealed for 2 h at 700 °C; all of them have similar microstructure. The primary particle sizes are less than 100 nm for all specimens.

Figs. 6a–e show the current–voltage–power ( $I$ – $V$ – $P$ ) curves for the PCFCs with various cathodes in the temperature range of 500–700 °C. The open circuit voltages (OCVs) of C- and R-LSMN at 500–700 °C are listed in Table S3 together with the theoretical OCVs. All LSMN cells exhibit smaller OCV values than the theoretical ones at temperatures above 600 °C, attributed to the increased hole conductivity of BZCY442 electrolytes.<sup>37</sup> OCVs of C phase are slightly higher than those of R phase and LSCF6428. Particularly, C-LSMN7373 cell gives the similar OCV

(1.12 V) as the theoretical value (1.16 V) at 500 °C, while LSCF6428 cell show the OCV below 1.0 V, which implies that proton conductivity of the cathode reduces the migration of holes into electrolyte.

The power densities of the PCFCs with a C-LSMN cathode (Figs. 6a and b) are much higher than those with a R-LSMN cathode in both LSMN7391 and LSMN7373 at all temperatures (Figs. 6c and d). The peak power densities (PPDs) of the C-LSMN7391 and C-LSMN7373 cells at 700 °C are 708 and 992  $\text{mW cm}^{-2}$ , respectively. At 600 °C, the PPDs for C-LSMN7391 and C-LSMN7373 are 296 and 386  $\text{mW cm}^{-2}$ , respectively, which are two and three times greater than the values of the corresponding R-LSMN cells (84 and 100  $\text{mW cm}^{-2}$  at 600 °C), respectively (Fig. 7a; Table S4). Moreover, the PPD of the C-LSMN7373 cell is slightly higher than that of the cells with a widely-used cobaltite cathode LSCF6428 (373  $\text{mW cm}^{-2}$ ) at 600 °C (Figs. 6f and 7a).

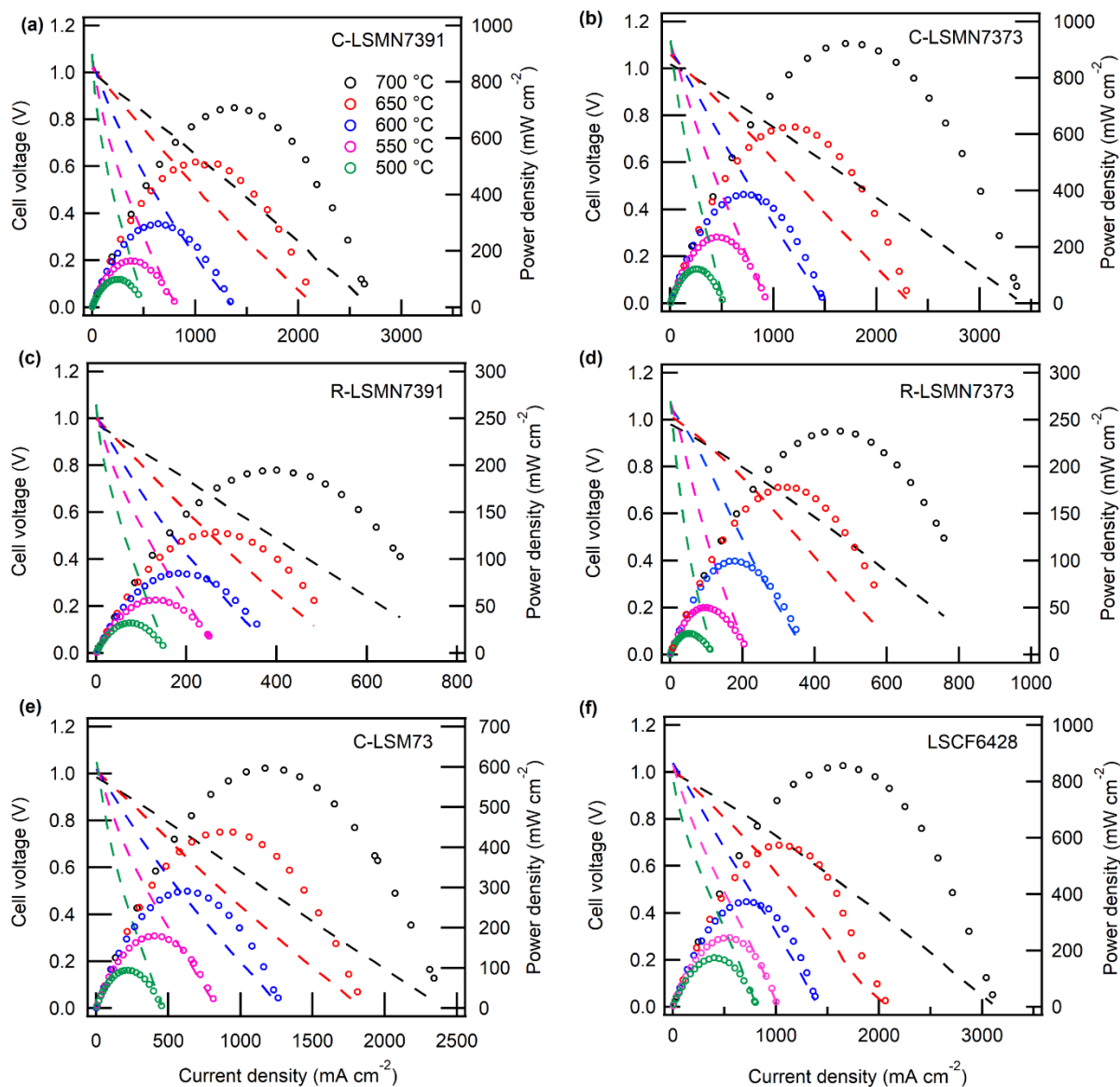
Recently, Choi *et al.* reported outstanding power outputs of a  $\text{BaZr}_{0.4}\text{Ce}_{0.4}\text{Y}_{0.1}\text{Yb}_{0.1}\text{O}_3$  (BZCYb4411)-based PCFC with  $\text{H}^+/\text{O}^{2-}/\text{e}^-$  triple-conducting  $\text{PrBa}_{0.5}\text{Sr}_{0.5}\text{Co}_{1.2}\text{Fe}_{0.8}\text{O}_3$  (PBSCF) cathode, in which the PPD exceeded 0.8  $\text{W cm}^{-2}$  at 600 °C.<sup>8</sup> Nevertheless, in most PCFCs comprising Zr-rich side  $\text{BaZr}_x\text{Ce}_{1-x-y}\text{Y}_y\text{O}_3$  solid solutions ( $x > 1-x-y$ ), the PPD is in the range of 0.1–0.3  $\text{W cm}^{-2}$  at 600 °C with cobalt-oxide cathodes.<sup>30–32,50–54</sup> Moreover, the performances of the fuel cells with Mn-based perovskite cathodes are normally much lower than those of the cells with cobalt-base cathodes at intermediate temperatures below 700 °C, because the relatively low oxide ion conductivity of the former limits the reaction rate at TPBs.<sup>27–29</sup> The C-LSMN cells exhibit similar or even superior fuel cell performances to the LSCF6428 ones, although the performance of the R-LSMN cells is inferior to the LSCF one (Fig. 7a; Table S4). This shows that the C-LSMN cathodes sufficiently decrease the cathodic polarization resistance owing to the formation of extended reaction area by proton conductivity.

Figs. S10a–e show the electrochemical impedance spectra of each cell at 700, 650, 600, 550, and 500 °C under OCV conditions. In general, the Nyquist plots of impedance responses of PCFCs have the  $x$ -intercept in a high-frequency region, which corresponds to electrolyte resistances ( $R_{\text{ohm}}$ ). After the intercept, they exhibit broad semi-arcs due to the interfacial polarization resistance at the cathode side,<sup>28</sup> and, the diameters of the arcs provide polarization resistance ( $R_p$ ) at the cathode side. The diameters of the semi arcs of the fuel cells with C-LSMN cathodes are several times smaller than those of the cells with R-LSMN ones, revealing that  $R_p$  of the former is much lower than that of the latter despite their similar chemical compositions. Fig. 7b shows  $R_p$  for various cathode-type cells, determined from the diameters of the impedance semi-arcs under OCV condition. The gap in  $R_p$  of the C- and R-phase cathodes tends to increase with decreasing temperatures. The  $R_p$  values of the C-LSMN7373 cell are 0.43 and 3.44  $\Omega \text{ cm}^2$  at 600 and 500 °C, respectively, which are much lower than the corresponding values of the R-LSMN7373 cell (1.14 and 14.01  $\Omega \text{ cm}^2$ ) by a factor of 2.6 and 4.1 at 600 and 500 °C, respectively. Similarly, the  $R_p$  values of the C-LSMN7391 cell are 0.68 and 3.60  $\Omega \text{ cm}^2$  at 600 and 500 °C, respectively, which are lower than the corresponding values of the

R-LSMN7391 cell. These features prove that the proton conductivity of C-LSMN cathodes efficiently lower the polarization resistances.

The C-LSM73 cathode exhibits higher  $R_p$  than the Ni-substituted ones, and thus, the PPD of the C-LSM73 cell (291 and 95  $\text{mW cm}^{-2}$  at 600 and 500  $^{\circ}\text{C}$ , respectively) is much lower than that with the C-LSMN7373 (Table S4; Figs. 6b, e, and 7a). The valence state of Ni cation is lower than the average value of Mn cations ( $> +3$ ) in all samples as confirmed by EXAFS, so that

the concentration of the oxygen vacancies must increase, thus increasing the concentrations of proton carriers with Ni substitution according to Equation (1). In fact,  $\Delta n$  of C-LSM73 (0.07) is lower than that of C-LSMN7373 (0.098; Table 1). C-LSMN7373 outperforms the C-LSM73 cell probably because of the higher proton conductivity.



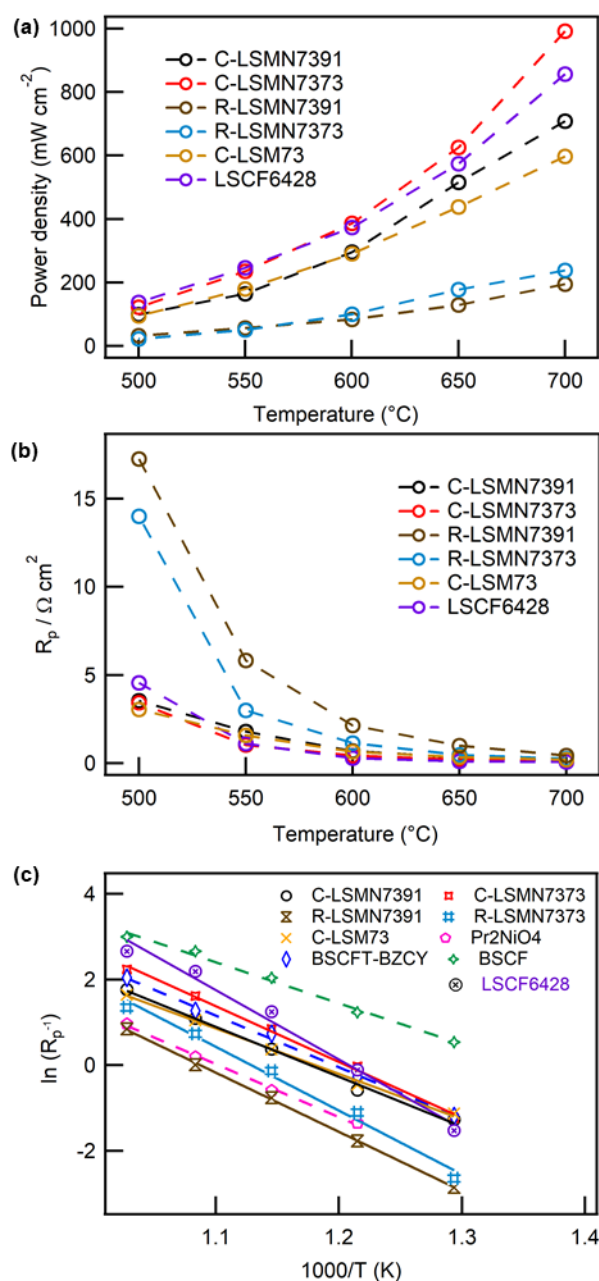
**Fig. 6**  $I$ - $V$  and  $I$ - $P$  curves of PCFCs with cathodes C-LSMN7391 (a), C-LSMN7373 (b), R-LSMN7391 (c), R-LSMN7373 (d), C-LSM73 (e), and LSCF6428 (f), in the temperature range of 500–700  $^{\circ}\text{C}$ .

Fig. 7c shows the Arrhenius plots of  $R_p^{-1}$  for BZCY442 cells. The activation energies ( $E_a$ ) related to  $R_p$  are 96.7 and 108  $\text{kJ mol}^{-1}$  for C-LSMN7391 and C-LSMN7373, respectively; these values are lower than those of the R-LSMN7391 (114.8  $\text{kJ mol}^{-1}$ ) and R-LSMN7373 (123.1  $\text{kJ mol}^{-1}$ ) cells (Table S4) and even lower than the widely used cathode materials, such as LSCF6428 (134.5  $\text{kJ mol}^{-1}$ ),  $\text{Pr}_2\text{NiO}_4$  (102.9  $\text{kJ mol}^{-1}$ ),<sup>31</sup> and  $\text{BaZr}_{0.4}\text{Ce}_{0.4}\text{Y}_{0.2}\text{O}_{3-\delta}\text{-Ba}_{0.5}\text{Sr}_{0.5}(\text{Co}_{0.8}\text{Fe}_{0.2})\text{Ti}_{0.9}\text{O}_{3-\delta}$  (BZCY-BSCFT;

100.2  $\text{kJ mol}^{-1}$ ).<sup>32</sup>  $R_p$  of C-LSMN7373 cell is slightly larger than those of LSCF6428 one at temperatures above 600  $^{\circ}\text{C}$  owing to relatively high  $E_a$  of the latter (Figs. 7b). Nevertheless, the former yield the similar PPDs as the latter, which is probably due to the relatively small hole leakage, as mentioned above (Figs. 7a and c).

Finally, the durability of C phase was examined by conducting galvanostatic operation of fuel cells under 800 mA

$\text{cm}^{-2}$  at 700 °C. The cell yielded a stable output without degradation for 35 hours (Fig. S11). XRD for the cathode after the durability test confirms that the oxide retains the cubic structure (Fig. S12). As mentioned above, the superior cathode performances of C-LSMN to R-LSMN highlights that proton conduction in C-LSMN series helps sufficiently lower the cathodic polarization resistance by extending the effective reaction areas from proton-electron-gas TPB zones to the overall electrode surface (Figs. 8a, b and c). In conclusion, cubic-type LSMN perovskites are beneficial to  $\text{H}^+/\text{O}^{2-}/\text{e}^-$  triple-conducting cathodes, making them a promising Co-free cathode material for advanced PCFCs operating at intermediate temperatures.



**Fig. 7** Plots of peak power densities (a) and cathodic polarization resistance ( $R_p$ ) as a function of the temperature (b). Arrhenius plots of the reciprocal of  $R_p$  for BZCY442-base PCFCs with various cathodes (c). In (c), the full lines are the ones measured in this work, whereas the dashed lines are the replots of data obtained previously for BSCF,<sup>33</sup> Pr<sub>2</sub>NiO<sub>4</sub>,<sup>31</sup> and BSCFT-BZCY,<sup>32</sup> respectively.

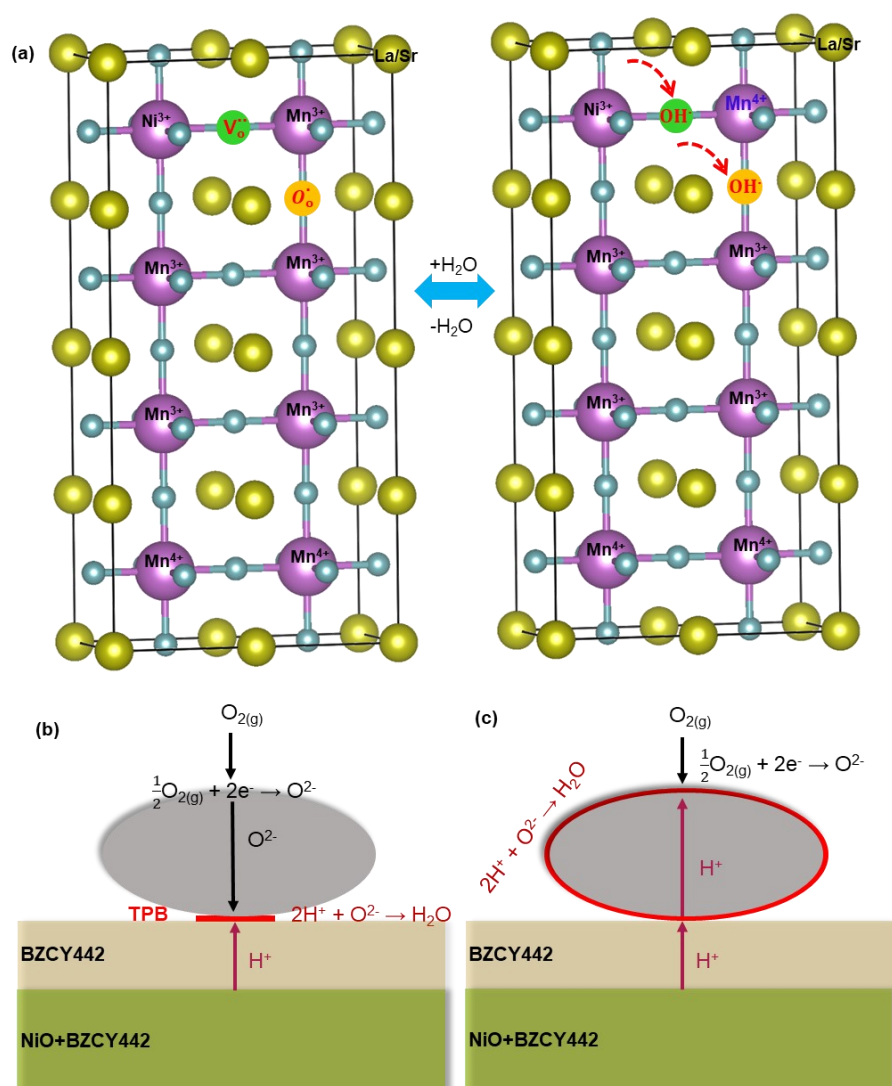


**Fig. 8** Mechanism of thermochemical hydration/dehydration reaction for C-LSMN (a), Schematic of cathode reaction of (b) O<sub>2</sub><sup>2-</sup>/e<sup>-</sup> mixed conductors and (c) H<sup>+</sup>/O<sub>2</sub><sup>2-</sup>/e<sup>-</sup> triple conducting conductors on PCFCs.

### 3 Experimental section

#### 3.1 Synthesis of La<sub>0.7</sub>Sr<sub>0.3</sub>Mn<sub>1-x</sub>Ni<sub>x</sub>O<sub>3-δ</sub>

La<sub>0.7</sub>Sr<sub>0.3</sub>Mn<sub>1-x</sub>Ni<sub>x</sub>O<sub>3-δ</sub> (LSMN;  $x = 0.1, 0.3$ ) fine powders were synthesized via a citrate precursor route reported elsewhere.<sup>35,55</sup> First, the required amounts (based on desired stoichiometry) of La(NO<sub>3</sub>)<sub>3</sub>·6H<sub>2</sub>O, Sr(NO<sub>3</sub>)<sub>2</sub>, Mn(NO<sub>3</sub>)<sub>2</sub>·6H<sub>2</sub>O, and Ni(NO<sub>3</sub>)<sub>2</sub>·6H<sub>2</sub>O (all from High Purity Chemicals, 99.99%) were completely dissolved in Milli-Q H<sub>2</sub>O. Citric acid (CA; C<sub>6</sub>H<sub>8</sub>O<sub>7</sub>·H<sub>2</sub>O) was then added as a chelate agent in a mole ratio of CA:LSMN = 2:1 (0.04 mol:0.02 mol). Next, the citrate solution was heated while vigorously stirring at 60 °C for 2 or 3 h to evaporate H<sub>2</sub>O and promote polymerization. Thus, we obtained gelatinous products. Deep color precursors were obtained by calcination of the gel at 500 °C for 1 h under air. Finally, precursors were annealed in a tube furnace at 800 and 1000 °C for 15 h under

pure O<sub>2</sub> atmosphere. The samples thus prepared were kept in air at 100 °C overnight for the hydration.

#### 3.2 Fabrication of PCFCs

The anode-supported PCFCs were fabricated by solid-state reactive sintering with a sintering aid of Zn(NO<sub>3</sub>)<sub>2</sub> as reported elsewhere.<sup>50</sup> BaCO<sub>3</sub> (High Purity Chemicals, 99.95%), ZrO<sub>2</sub> (High Purity Chemicals, 98%), CeO<sub>2</sub> (High Purity Chemicals, 99.99%), and Y<sub>2</sub>O<sub>3</sub> (High Purity Chemicals, 99.99%) with 3.56 wt% of Zn(NO<sub>3</sub>)<sub>2</sub>·6H<sub>2</sub>O (Wako chemicals, 99.9%) were ball-milled in ethanol for 48 h and subsequently dried at 80 °C to obtain precursor powders of BaZr<sub>0.4</sub>Ce<sub>0.4</sub>Y<sub>0.2</sub>O<sub>3</sub> (BZCY442, ~0.025 mol). This precursor powder is denoted by Pre-1. Moreover, the precursor powders for the anode supports (noted by Pre-2) were prepared by mixing Pre-1 and NiO at a weight ratio of 40:60 (BZCY442:NiO) in ethanol and ball-milled for 48 h. The Pre-2 powders were uniaxially pressed under 20 MPa and subsequently pressed isostatically under a hydrostatic pressure of 100 MPa. Thus, we obtained green pellets (~12 mm diameter,

~1.2 mm thickness) of anode-supported precursors. The precursor layers of the electrolyte films were spin-coated on both surfaces of the green pellets with sols, which were prepared by dispersing Pre-1 into a solution containing dispersant (20 wt% polyethyleneimine ( $M_w$  28000) dissolved in  $\alpha$ -terpineol) and binder (5 wt% surfactant dissolved in  $\alpha$ -terpineol). These pellets were co-sintered at 1400 °C for 12 h at air atmosphere, resulting in a compact ceramic disc with ca. 9 mm  $\phi$   $\times$  1 mm *d*. The back side of the sintered discs was polished with a mechanical grinder and was then applied with Pt paste as a current collector attached with a gold wire (0.1 mm  $\phi$ ). Finally, an LSMN button electrode was deposited on the electrolyte as a porous cathode by screen printing.

### 3.3 Characterization

The phase purity was verified by X-ray powder diffraction (XRD; Rigaku, Ultima IV) using Cu  $K\alpha$  radiation (40 kV, 20 mA) in a  $2\theta$  range of 5–90°. The scan rate and  $2\theta$  step were 5° min<sup>-1</sup> and 0.02°, respectively. The XRD patterns were refined by the Rietveld method using the GSAS software over the  $2\theta$  range of 20–80°. Scanning electron microscopy (FESEM; SIGMA500, ZEISS) was performed to measure the microstructure of the PCFCs.

Thermogravimetric (TG) analyses were performed using a STA2500 thermogravimetric analyzer (Netzsch).<sup>35</sup> The measurement was carried out with approximately 20 mg of the LSMN specimen at temperatures ranging from room temperature (RT) to 1000 °C at a ramp rate of 5 °C min<sup>-1</sup> under a flow of dry/wet Ar and air atmosphere at 50 sccm. Ar gas with added O<sub>2</sub> (10 ppm) was used as Ar gas in order to fix  $p_{O_2}$  of wet gas.<sup>56</sup> Dry air was prepared by mixing a flow of pure O<sub>2</sub> (99.9%; 10 sccm) and Ar (40 sccm) in the ratio of 1/4 (v/v). Wet gases were prepared by bubbling through a water bath at -8, 5, and 20 °C at a flow rate of 50 sccm. The resultant gases have water partial pressures ( $p_{H_2O}$ ) of 0.003, 0.009, and 0.023  $p_0$  ( $p_0 = 101.3$  kPa).

The *in situ* extended X-ray absorption fine structure (EXAFS) for the Mn K-edge and Ni K-edge was obtained on the BL01B1 station of *Spring-8* facility, Japan Synchrotron Radiation Research Institute (JASRI). The sample placed in a temperature- and atmosphere-controllable cell was heated to 415 °C at a heating rate of 10 °C min<sup>-1</sup> in dry air (He/O<sub>2</sub> = 4/1 (v/v), flow rate: 50 mL/min). An Si (111) double-crystal monochromator was used. The incident and transmitted X-rays were monitored in ionization chambers filled with N<sub>2</sub> and 85% N<sub>2</sub> + 15% Ar. Quick EXAFS in the continuous scanning mode was recorded from 6520 to 6600 eV (5 min scan<sup>-1</sup>). All the samples were mixed with boron nitride (BN) powder to achieve an appropriate absorbance at the edge energy. The EXAFS data were processed using the IFEFFIT software package (Athena and Artemis).

*In situ* transmittance IR spectra was conducted by FT-IR-4600 Fourier Transform Infrared Spectrometer from JASCO. *In situ* measurements were performed in a gas-sealed optical cell with an antireflective glass window under controlled atmospheric and thermal conditions. The impedance spectra of the PCFCs were obtained with a Solartron 1260A frequency response analyzer implemented with a Solartron 1287

potentiostat in the frequency range of 10<sup>6</sup>–0.1 Hz with an AC amplitude of 30 mV under an open circuit voltage (OCV) condition. The current–voltage ( $I$ – $V$ ) and current–power ( $I$ – $P$ ) characteristics were recorded on the same apparatus.

## 4 Conclusions

In summary, we demonstrated that cubic-type La<sub>0.7</sub>Sr<sub>0.3</sub>Mn<sub>1-x</sub>Ni<sub>x</sub>O<sub>3- $\delta$</sub>  (C-LSMN) are beneficial to H<sup>+</sup>/e<sup>-</sup>/O<sup>2-</sup> triple conducting cathodes intended for PCFCs operating at intermediate temperatures. C-LSMN undergoes thermochemical hydration at approximately 400 °C in air by gaining proton carriers of 0.2 molar fraction, which is quite similar to the concentration of the widely-used proton conducting ceramic BaCe<sub>0.9</sub>Y<sub>0.1</sub>O<sub>3</sub>. However, rhombohedral-type La<sub>0.7</sub>Sr<sub>0.3</sub>Mn<sub>0.7</sub>Ni<sub>0.3</sub>O<sub>3</sub> (*R*-LSMN) does not undergo hydration because of the lack of oxygen vacancies. Accordingly, BaZr<sub>0.4</sub>Ce<sub>0.4</sub>Y<sub>0.2</sub>O<sub>3</sub> thin film fuel cells with C-LSMN cathodes exhibited a lower polarization resistance than the analogous cells with the *R*-LSMN cathodes by one order of magnitude in the temperature range of 500–600 °C, because the effective cathode reaction areas could be extended from triple phase boundaries to the overall cathode surface through enhanced proton conduction. In fact, the cell with cubic-type La<sub>0.7</sub>Sr<sub>0.3</sub>Mn<sub>0.7</sub>Ni<sub>0.3</sub>O<sub>3</sub> exhibited a similar cathodic polarization resistance as the cell with the widely-used LSCF6428 cathode and yielded peak power densities of 122 and 386 mW cm<sup>-2</sup> at 500 and 600 °C, respectively. In conclusion, cubic-type La<sub>0.7</sub>Sr<sub>0.3</sub>Mn<sub>1-x</sub>Ni<sub>x</sub>O<sub>3- $\delta$</sub>  is a promising Co-free cathode material for PCFCs operating at intermediate temperatures.

## Conflicts of interest

There are no conflicts to declare.

## Acknowledgements

This work was supported by the JST MIRAI “Realization of a low carbon society, global issue”, No. JPMJM17E7; JSPS KAKENHI: Grant-in-Aid for Scientific Research (B), No.18H02066; and the “Research and Development Initiative for Science Innovation of New Generation Battery (RISING2 Project)” of the New Energy and Industrial Technology Development Organization (NEDO), Japan. XAFS measurements were performed with the approval of SPring-8 (No.2018B1112).

## Notes and references

- 1 J. G. Lee, J. H. Park and Y. G. Shul, *Nat. Commu.* 2014, **5**, 4045;
- 2 S. Choi, S. Yoo, J. Kim, S. Park, A. Jun, S. Sengodan, J. Kim, J. Shin, H. Y. Jeong and Y. Choi, *Sci. Rep.* 2013, **3**, 2426;
- 3 C. Duan, J. Tong, M. Shang, S. Nikodemski, M. Sanders, S. Ricote, A. Almansoori and R. O’Hayre, *Science* 2015, **349**, 1321;
- 4 D. Pergolesi, E. Fabbri, A. D. Epifanio, E. D. Bartolomeo, A. Tebano, S. Sanna, S. Licoccia, G. Balestrino and E. Traversa, *Nat. Mater.* 2010, **9**, 846.

- 5 Y. Yamazaki, R. H. Sanchez, S. M. Haile, *Chem. Mater.* 2009, **21**, 2755.
- 6 R. Peng, T. Wu, W. Liu, X. Liu and G. Meng, *J. Mater. Chem.* 2010, **20**, 6218.
- 7 D. A. Medvedev, J. G. Lyagaeva, E. V. Gorbova, A. K. Demin and P. Tsiakaras, *Prog. Mater. Sci.* 2016, **75**, 38.
- 8 S. Choi, C. J. Kucharczyk, Y. Liang, X. Zhang, I. Takeuchi, H. I. Ji and S. M. Haile, *Nat. Energy* 2018, **3**, 202.
- 9 H. An, H. W. Lee, B. K. Kim, J. W. Son, K. J. Yoon, H. Kim, D. Shin, H. I. Ji and J. H. Lee, *Nat. Energy* 2018, **3**, 870.
- 10 K. Bae, D. H. Kim, H. J. Choi, J. W. Son and J. H. Shim, *Adv. Energy Mater.* 2018, **8**, 1801315.
- 11 S. Nien, C. Hsu, C. Chang and B. Hwang, *Fuel cells* 2011, **11**, 178.
- 12 K. Kreuer, *Solid State Ionics* 1999, **125**, 285.
- 13 K. D. Kreuer, W. Münch, A. Fuchs, U. Klock and J. Maier, *Solid State Ionics* 2001, **145**, 295.
- 14 M. Shang, J. Tong and R. O'Hayre, *RSC Adv.* 2013, **3**, 15769.
- 15 J. Tong, W. Yang, B. Zhu and R. Cai, *J. Membrane Sci.* 2002, **203**, 175.
- 16 A. Grimaud, F. Mauvy, J. Bassat, S. Fourcade, L. Rocheron, M. Marrony and J. Grenier, *J. Electrochem. Soc.* 2012, **159**, B683.
- 17 D. Han, Y. Okumura, Y. Nose and T. Uda, *Solid State Ionics* 2010, **181**, 1601.
- 18 J. Kim, S. Sengodan, G. Kwon, D. Ding, J. Shin, M. Liu and G. Kim, *ChemSusChem*, 2014, **7**, 2811–2815.
- 19 K. Bae, D. Jang, H. Choi, D. Kim, J. Hong, B. Kim, J. Lee, J. W. Son and J. H. Shim, *Nat. Commun.* 2017, **8**, 14553.
- 20 C. Duan, D. Hook, Y. Chen, J. Tong and R. O'Hayre, *Energy Environ. Sci.* 2017, **10**, 176.
- 21 J. Dailly, S. Fourcade, A. Largeteau, F. Mauvy, J. C. Grenier and M. Marrony, *Electrochim. Acta* 2010, **55**, 5847.
- 22 Y. Lin, R. Ran and Z. Shao, *Int. J. Hydrog. Energy* 2010, **35**, 8281.
- 23 K. Kravchyk, E. Quarez, C. Solís, J. Serra and O. Joubert, *Int. J. Hydrog. Energy* 2011, **36**, 13059.
- 24 B. Hua, N. Yan, M. Li, Y. Q. Zhang, Y. F. Sun, J. Li, T. Etsell, P. Sarkar, K. Chuang and J. L. Luo, *Energy Environ. Sci.* 2016, **9**, 207.
- 25 S. Choi, T. C. Davenport and S. M. Haile, *Energy Environ. Sci.* 2019, **12**, 206.
- 26 Y. Niu, W. Zhou, J. Sunarso, L. Ge, Z. Zhu and Z. Shao, *J. Mater. Chem.* 2010, **20**, 9619.
- 27 Y. Okuyama, N. Ebihara, K. Okuyama and Y. Mizutani, *ECS Trans.* 2009, **68**, 2545.
- 28 J. S. Park, J. H. Lee, H. W. Lee and B. K. Kim, *ECS Trans.* 2009, **25**, 795.
- 29 D. K. Lim, H. N. Im, B. Singh and S. J. Song, *J. Electrochem. Soc.* 2015, **162**, F547.
- 30 Y. Guo, Y. Lin, R. Ran and Z. Shao, *J. Power Sources* 2009, **193**, 400.
- 31 N. Nasani, D. Ramasamy, S. Mikhalev, A. V. Kovalevsky and D. P. Fagg, *J. Power Sources* 2015, **278**, 582.
- 32 L. Bi, E. Fabbri and E. Traversa, *Electrochem. Commun.* 2012, **16**, 37.
- 33 Y. Liu, Y. Guo, R. Ran and Z. Shao, *J. Membrane Sci.* 2013, **437**, 189.
- 34 G. Wang, T. Xu, S. Wen and M. Pan, *Sci. China: Chem.* 2015, **58**, 871.
- 35 N. Wang, S. Hinokuma, T. Ina, H. Toriumi, M. Katayama, Y. Inada, C. Zhu, H. Habazaki and Y. Aoki, *Chem. Mater.* 2019, **31**, 8383.
- 36 S. Bishop, D. Marrocchelli, W. Fang, K. Amezawa, K. Yashiro and G. W. Watson, *Energy Environ. Sci.* 2013, **6**, 1142.
- 37 T. Norby and Y. Larring, *Curr. Opin. Solid St. M.* 1997, **2**, 593.
- 38 D. K. Lim, M. B. Choi, K. T. Lee, H. S. Yoon, E. Wachsman and S. J. Song, *Int. J. Hydrog. Energy* 2011, **36**, 9367.
- 39 S. J. Song, E. D. Wachsman, S. E. Dorris and U. Balachandran, *Solid State Ionics* 2002, **149**, 1.
- 40 C. J. Park, H. W. Ryu, J. H. Moon, J. S. Lee and S. J. Song, *Ceram. Inter.* 2009, **35**, 1769.
- 41 C. R. Fell, D. Qian, K. J. Carroll, M. Chi, J. L. Jones, Y. S. Meng, *Chem. Mater.* 2013, **25**, 1621.
- 42 J. Rana, M. Stan, R. Kloepsch, J. Li, G. Schumacher, E. Welter, I. Zizak, J. Banhart and M. Winter, *Adv. Energy Mater.* 2014, **4**, 1300998.
- 43 F. Farges, *Phys. Rev. B* 2005, **71**, 155109.
- 44 C. Henderson, J. Charnock, J. Smith and G. Greaves, *Am. Mineral.* 1993, **78**, 477.
- 45 A. Gaur, B. D. Shrivastava and H. Nigam, *Proceedings of the Indian National Science Academy* 2013, **79**, 921.
- 46 B. Wei, Z. Lü, X. Huang, M. Liu, N. Li and W. Su, *J. Power Sources* 2008, **176**, 1.
- 47 J. Mizusaki, N. Mori, H. Takai, Y. Yonemura, H. Minamiue, H. Tagawa, M. Dokiya, H. Inaba, K. Naraya and T. Sasamoto, *Solid state ionics* 2000, **129**, 163.
- 48 B. Lengeler, P. Eisenberger, *Phys. Rev. B*, 1980, **21**, 4507-4520.
- 49 J. Kuo and H. Anderson, *J. Solid State Chem.* 1989, **83**, 52-60.
- 50 S. Jeong, T. Kobayashi, K. Kuroda, H. Kwon, C. Zhu, H. Habazaki and Y. Aoki, *RSC Adv.* 2018, **8**, 26309.
- 51 J. Xiao, W. Sun, Z. Zhu, Z. Tao and W. Liu, *Mater. Lett.* 2012, **73**, 198.
- 52 C. L. Tsai, M. Kopczyk, R. Smith and V. H. Schmidt, *Solid State Ionics* 2010, **181**, 1083.
- 53 Y. Liu, R. Ran, M. O. Tade and Z. Shao, *J. Membrane Sci.* 2014, **467**, 100.
- 54 W. Sun, L. Yan, Z. Shi, Z. Zhu and W. Liu, *J. power sources* 2010, **195**, 4727.
- 55 Y. Aoki, E. Tsuji, T. Motohashi, D. Kowalski and H. Habazaki, *J. Phys. Chem. C* 2018, **122**, 22301.
- 56 R. Zohourian, R. Merkle, G. Raimondi and J. Maier, *Adv. Funct. Mater.* 2018, **28**, 1801241.
- 57 D. Poetzsch, R. Merkle and J. Maier, *Faraday Discuss.* 2015, **182**, 129.
- 58 D. Poetzsch, R. Merkle and J. Maier, *Phys. Chem. Chem. Phys.* 2014, **16**, 16446.